PAPER

Check for updates

Photophysics of proton transfer in hydrazides: a combined theoretical and experimental analysis towards OLED device application†

Makesh Mohan, [ID] [a] M. N. Satyanarayan*[a] and Darshak R. Trivedi [ID] *[b]

Hydrazides generate phototautomers and thus, a mechanistic interpretation to uncover the excited state dynamics of such systems is highly necessary to theorize principles based on experimental speculations. Accordingly, focus on the proton transfer barrier, which is a questionable step-wise or hypothetical simultaneous double proton transfer on structurally favored species, is quintessential; however, to the best of our knowledge, theoretical insights into such findings remain rare. Thus, **TX**, **PX** and **FX** (where X = 2 and 3) were designed and synthesized by incorporating hydrazides, which exhibit the phenomenon of excited state intramolecular proton transfer (ESIPT). Some of the molecules exhibited electroluminescence when employed as an active emitter material in fabricated OLED devices. Theoretical predictions support the presence of extended conjugation in **TX**, **PX** and **FX** (where X = 2 and 3) to support ESIPT efficiently in comparison with **TX**, **PX** and **FX** (where X = 1). The solvatochromic study revealed that **TX**, **PX** and **FX** (where X = 2 and 3) exhibit a distinct double peak in THF solvent, characteristic of ESIPT. Interestingly, for some of the molecules, emission in thin film form showed a double peak, which indicates ESIPT in the solid state. However, it was found that aggregation induced emission (AIE) was inactive in these molecules. The geometrical attributes of the molecules and the nature of electronic orbital distribution well underline the principle supporting excited state proton translocation. The theoretically estimated energy transitions exhibited good correlation with the experimental results. Also, the potential energy scans revealed the molecules possess a lower forward barrier at their excited state in comparison with that of their ground state, promoting ESIPT. The potential energy surface scans performed on structurally favored species confirmed the impossible double proton transfer and highly difficult step-wise double proton transfer.

Introduction

Tautomerism in hydrazides in the excited state is characterized by translocation of a proton from a proton donor (–NH) to a proton acceptor (–C=O) moiety with pre-linked intramolecular hydrogen bonding.[1] The energy gap between the locally excited state and relaxed excited state of the system is responsible for efficient proton transfer and the gradient of the surface

[a] *Optoelectronics Laboratory, Department of Physics, National Institute of Technology Karnataka (NITK) Surathkal, Mangalore – 575025, India. E-mail: satya_mn@nitk.edu.in, darshak_rtrivedi@yahoo.co.in; Tel: +91-824-2473295*

[b] *Supramolecular Chemistry Laboratory, Department of Chemistry, National Institute of Technology Karnataka (NITK) Surathkal, Mangalore – 575025, India*

† Electronic supplementary information (ESI) available: Characterization results of all the molecules, including FTIR, ^{1}H-NMR, ESI-MS, and optical characterization includes UV-vis, PL and AIE studies. DFT results together with the potential energy curves of a few of the molecules are provided. See DOI: 10.1039/c9nj01503e

connecting these two points provides the activation kinetics for the system.[2–7] Tautomer structures exhibit exceptional photophysical properties, which are highly unique for systems supporting excited state intramolecular proton transfer (ESIPT).[8–11] The intramolecular hydrogen bond in its normal form (N), when excited (N*) triggers proton transfer, leading to the formation of a structural transformation tautomer (T*). The tautomer T* relaxes to its tautomer ground state (T) either by fluorescence emission or internal conversion, ensuring the tautomer rolls back to the normal (N) form *via* reverse ground-state proton transfer (RGSPT), realizing a four level photocyclic process (N → N* → T* → T → N),[12–31] as presented in the Fig. 1. Tautomeric emissions are often highly red-shifted from normal absorption, leading to large Stokes shifts, which rule out the probability of self-absorption of generated photons.[12,16–18,25–34] Dual fluorescence emission is highly unusual in molecules exhibiting ESIPT, which is highly fascinating for practical applications in UV filters,[35–38] fluorescence sensors[16,35–46] and aggregation-induced emissive materials.[47–59]
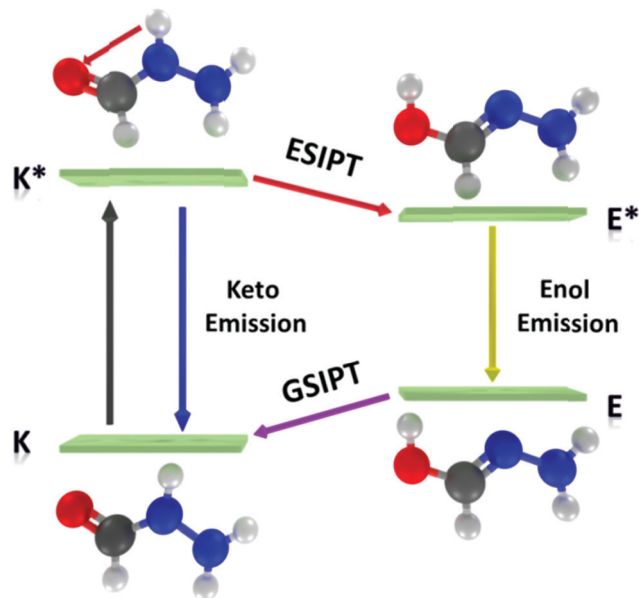
Fig. 1 Generic mechanism of keto–enol tautomerism exhibited in acid hydrazides.

Fine tuning and systematic control over the dual emission energies has opened up research in developing single molecules that generate white light emission for OLED device applications.[47,60–62]

Hydrazides are a class of organic systems that supports the thermodynamically stable keto form and kinetically inert enolic tautomer upon photoexcitation. One of the possible reasons for this is that the –C═N group possesses a low bond energy of 615 kJ mol^{-1}, making the hydrazine N–H bond stronger, which results in the stable keto form at its ground state. The introduction of heterocyclic rings viz. thiophene, furan, and pyridine tends to alter the electronic density of the system, which in turn effectively governs the ESIPT of the system.[63] The photophysical attributes of the studied substituted hydrazides were enhanced by covalently linking thiophene and bithiophene moieties to investigate their practical applications as solid state emitters in OLEDs. The ease of synthetic modification and environmental stability of thiophene- and bithiophene-based materials have demonstrated their potential as versatile conjugated systems for practical applications.[64,65] Hence, here, we attempted to study the nature of excited state properties with meticulous initiation of proton transfer by incorporating extended conjugation into structures. Theoretical predictions validate the presence of extended conjugation to specifically activate proton transfer efficiently in comparison with **T1, P1** and **F1**. To the best of our knowledge, theoretical aspects uncovering the remarkable excited state proton transfer properties of hydrazides remain a topic of discussion. Information relating to structures that favor simultaneous double proton transfer or step-wise double proton transfer is highly necessary to understand some of the underlying principles relating to the kinetics of hydrazides.

Experimental

Materials and methods

All chemicals used were procured from Sigma-Aldrich and used as received without further purification. All solvents were purchased from SD Fine, India, and were of HPLC grade and used without further distillation. Infrared spectra were recorded on a Bruker Apex FTIR spectrometer. UV-vis spectra of all the molecules were measured using an Ocean Optics SD2000 spectrometer, and photoluminescence studies were carried out using a Horiba Jobin Yvon spectrofluorometer. Cyclic voltammograms were recorded on an IVIUM electrochemical workstation at a scan rate of 20 mV s^{-1} in the maximum potential range of -5 V to 5 V. Device fabrication was performed using physical thermal vapor deposition at a base pressure of 5×10^{-6} Torr. Layers were deposited onto patterned indium-tin oxide (ITO) coated glass substrates with a sheet resistance of 15 Ω square cm^{-1}. ITO substrates were cleaned with soap solution followed by ultra-sonication in isopropyl alcohol for 20 min, which was followed by vapor degreasing using acetone. UV-ozone treatment was performed on the ITO substrates for 20 min to enhance their work function. The layers as per the device architecture were sequentially deposited under high vacuum condition. The deposition rate of organic materials was kept at 0.1 Å s^{-1} to 0.5 Å s^{-1}, and for aluminium the rate was maintained at 5 Å s^{-1}. The total active device area was measured to be 1.6 mm^2. EL spectra and current density–voltage–lumens (J–V–L) characteristics of the devices were measured using a Keithley source meter (Keithley 2400) and calibrated Si photodiode (SM1PD2A) equipped with an integrating sphere. All measurements were carried out at room temperature under ambient conditions.

Computational calculation for all the molecules was conducted using the Gaussian 09 package.[66] Ground state calculations S_0 were carried out using DFT Becke's three-parameter hybrid exchange function with the Lee–Yang–Parr gradient-corrected correlation functional (B3LYP)[67,68] with the 6-311+G(d,p)[69,70] basis set and excited state calculations S_1 were carried out using the TD-DFT Coulomb-Attenuated Method B3LYP[71] method with the same basis set used for the ground state. The self-consistent field (SCF) convergence thresholds pertaining to energy minimizations for both the S_0 and S_1 state optimization was set to 10^{-6}. The effect of solvent on the energy parameters of the system was studied using the self-consistent reaction field based on the polarizable continuum model (PCM)[72] using the integral equation formalism variant (IEFPCM).[73–77] The IEFPCM model studies the effect of solvent by placing the solute in a cavity of overlapping solvent, which reproduces the electrostatic potential arising due to the polarized dielectric created by the apparent charges surrounding the solute.[78] The functional was selected in accordance with previous numerous benchmarks validating its accuracy in predicting ground state energies and excited state energies.[79–81] Initially, ground state optimizations were carried out at vacuum and the resultant geometry was further optimized in the solvent medium. The experimental results revealed the ESIPT mechanism occurred in solvents of lower dielectric medium, and thus to corroborate this effect theoretically, THF was chosen as the

solvent medium for all the theoretical calculations. Frequency calculations were performed for the optimized geometry to confirm this geometry corresponds to a true local minimum on the S_0 and S_1 potential energy surface. Geometry optimizations were carried out without any constraints on bond lengths, bond angles or dihedral angles; however, these constraints were used while constructing potential energy surfaces (PESs) and potential energy curves (PECs). The PESs and PECs in the S_0 and S_1 states were scanned by constraining the O–H bond length fixed for a series of values with other degrees of freedom optimized without any constraint. The calculation of vertical excitation energy of the first six singlet excited states, S_1, was estimated from the ground state optimized structure based on TDDFT with the IEFPCM solvation model. The optimized geometry and the electronic orbital distribution of all the molecules were visualized using the Avogadro software.[82]
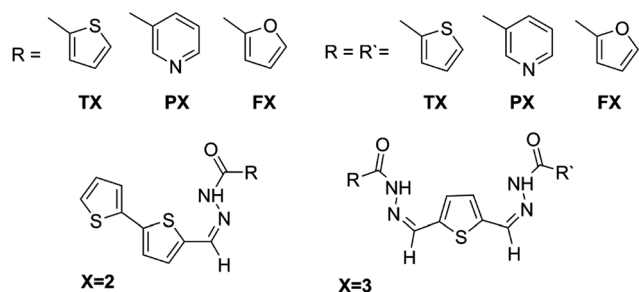
Synthesis

Molecules **T2** [(E)-N′-([2,2′-bithiophen]-5-ylmethylene)thiophene-2-carbohydrazide], **P2** [(E)-N′-([2,2′-bithiophen]-5-ylmethylene)nicotinohydrazide] and **F2** [(E)-N′-([2,2′-bithiophen]-5-ylmethylene)-furan-2-carbohydrazide] were synthesized via the Schiff base condensation of 2,2′-bithiophene-5-carboxaldehyde (0.1 g, 0.51 mmol) with 2-thiophene carboxylic acid hydrazide (0.073 g, 0.51 mmol), nicotinic acid hydrazide (0.071 g, 0.51 mmol) and 2-furoic hydrazide (0.071 g, 0.51 mmol), respectively. Molecules **T3** [N′,N′′′-((1E,1′E)-thiophene-2,5-diylbis(methaneylylidene))bis-(thiophene-2-carbo hydrazide)], **P3** [N′,N′′′-((1E,1′E)-thiophene-2,5-diylbis(methaneylylidene))di(nicotinohydrazide)] and **F3** [N′,N′′′-((1E,1′E)-thiophene-2,5-diylbis(methaneylylidene))bis-(furan-2-carbo hydrazide)] were synthesized via the Schiff base condensation of 2,5-thiophenedicarboxaldehyde (0.1 g, 0.71 mmol) with 2-thiophene carboxylic acid hydrazide (0.2 g, 1.42 mmol), nicotinic acid hydrazide (0.196 g, 1.43 mmol) and 2-furoic hydrazide (0.18 g, 1.43 mmol), respectively. All the reactions were performed in ethanol in the presence of acetic acid as a catalyst. The structures of the representative molecules are shown in Scheme 1.

Results and discussion

Photophysical studies

The UV-vis spectra of all the molecules exhibited two main bands. The lowest lying absorption band centered at 360–370 nm can be

attributed to the π–π* transition of the aromatic rings. The second band at 400–450 nm corresponds to the n–π* transition of the C=O and C=N groups. The second band is split and broad, indicating intramolecular hydrogen bonding, which induces the –NH proton to be acidic and the carbonyl oxygen to be basic with respect to their ground state driving the proton-transfer reaction.[83] The UV-vis spectra of all the molecules in solvents with different dielectric constants are provided in [S19–S24, ESI†]. The observed bathochromic shift in the polar protic solvents is indicative of strengthening of the intermolecular hydrogen bonding between the solute and solvent molecules in their excited state.[84]
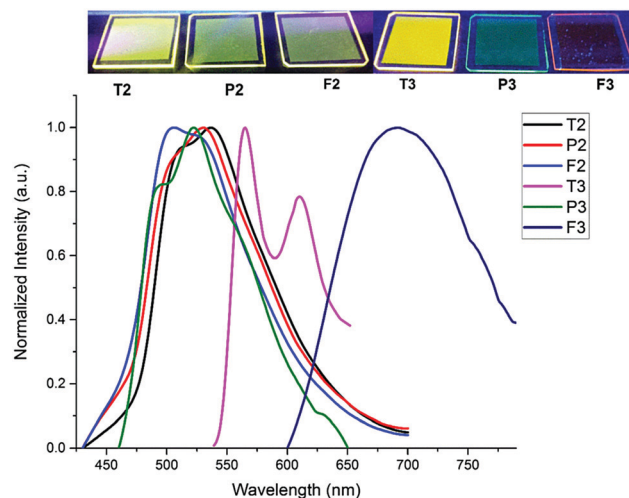
Fluorescence emission studies were carried out in solvents of varying polarities to gain a better understanding of the nature of ESIPT in different solvents. The molecules in the series exhibited a general photoluminescence response of a double peak, which is related to keto (k*) and enol (e*) emissions characterized by a four-level photo cyclic process triggered due to intramolecular H-bonding. The photophysical property of the molecules in solvents of varying polarity is summarized in Table 1 and the spectra are provided in [S26–S31, ESI†]. Specifically, THF possessing a very low dielectric constant supports ESIPT with a distinct keto–enol emission for all the molecules in the series, as evident from their spectra. The conjugation-enhanced structural backbone of **T3**, **P3** and **F3** with acyl substituted hydrazides on both the arms showed a red-shifted keto emission in all the solvents in comparison with the others in the series. Methanol, a polar protic solvent has a tendency to form H-bonding with solute molecules; thus, the molecules in the series did not show dual emission in methanol. In polar solvents, besides intramolecular H-bonding, intermolecular H-bonding is quite probable between solute and solvent molecules.[28] Polar solvents acting as hydrogen bond acceptors can impede the ESIPT process by bonding with the proton donor species, resulting in suppression of the tautomer emission.[85] The emission energy of organic systems is based on the nature of H-bonding occurring between the solute and solvent molecules.[79,86] If the solvent induces a bathochromic shift in the emission energy, this indicates strengthening of the intermolecular hydrogen bonds; whereas, a hypsochromic shift indicates weakening of the hydrogen bonds.[84] This was highly prevalent in this study, where the molecules showed a red-shifted emission in comparison with other solvents, superseding the trend, which was expected. All the molecules showed a bathochromic emission wavelength from THF to ACN, excluding methanol, exhibiting positive solvatochromic behavior. Polar solvents inducing positive solvatochromism in solute–solvent interactions substantiates better stabilization of the excited state compared to that of the ground state. Consequently, redistribution of the charges occur, supporting multi-dimensional intramolecular charge transfer (MDICT) between the core and peripheral moieties.[87] **T2**, **F2**, and **F3** exhibited a positive solvatochromic effect in DMF in contrast with the others in the series, which exhibited negative solvatochromism. **P2** and **P3** possessing a nicotinic hydrazide moiety exhibited similar emission patterns, supporting positive solvatochromism, neglecting the slight changes due to the close dielectric constants of ACN and DMF. **F3** exhibited a peculiar emission

Scheme 1 Synthesized molecular structures of **T2**, **P2**, **F2**, **T3**, **P3** and **F3**.

Table 1 Photophysical parameters of the molecules in solvents of different polarities

λ_{abs} (nm)	λ_{exe} (nm)	λ_{emi} (nm) Keto (k)	Enol (e)	Normal Stokes shift (nm)	Large Stokes shift (nm)
THF					
T2 372, 438	372	418	450	46	32
P2 368, 435	368	413	444	45	31
F2 372, 436	372	415	441	43	26
T3 382, 401, 449	382	425	447	43	22
P3 373, 388, 438	373	417	451	44	34
F3 407	407	456	484	49	28
MeOH					
T2 378, 435	378	461	—	83	—
P2 370, 435	370	463	—	93	—
F2 370, 435	370	450	—	80	—
T3 381, 400, 443	381	506	—	125	—
P3 380, 391, 433	391	481	—	90	—
F3 413	413	535	—	122	—
ACN					
T2 372, 440	372	422	450	50	28
P2 370, 432	370	423	450	53	27
F2 364, 440	364	446	—	82	—
T3 378, 396, 438	378	510	—	132	—
P3 370, 390, 434	370	465	486	95	21
F3 405	405	517	—	112	—
DMF					
T2 385, 440	385	462	490	77	28
P2 376, 440	376	420	460	44	40
F2 376, 440	376	459	483	83	24
T3 387, 402, 455	387	484	505	97	21
P3 378, 398, 441	379	463	487	84	24
F3 410	410	518	—	108	—
DMSO					
T2 379, 439	379	432	461	53	29
P2 374, 439	374	427	453	53	26
F2 374, 439	374	426	451	52	25
T3 381, 448	381	455	—	74	—
P3 378, 446	378	478	503	100	25
F3 415	415	508	—	93	—

Fig. 2 Solid state PL spectra of the molecules. Inset shows their solid state emission under UV illumination.

and investigated for their photophysical responses. The solid state UV-vis spectra of all the molecules are provided in [S25, ESI†], and their fluorescence spectra shown in Fig. 2 with the inset showing their fluorescence emission under UV irradiation. The solid state photophysical parameters of the molecules are provided in Table 2. The solid state emission of **T2**, **P2**, **P3**, and **F2** exhibited a small Stokes shift between keto and enol emission. **T3** exhibited a clear well-resolved double peak with a yellow emission and **F3** exhibited a single emission peak centered at 690 nm with the highest normal Stokes shift of 270 nm. A large Stokes shift was only observed for **T3**, which exhibited a value of 106 nm; whereas, the rest of the molecules showed a value of $\sim$25 nm.

The fluorescence quantum yields (φ_S) were evaluated according to eqn (1), where Coumarin 153 in cyclohexane was considered as the reference (R) for **T3**, **P3**, and **F3**, while for **T2**, **P2** and **F2**, 9,10-diphenyl anthracene was taken as the reference. The samples for which QY needs to be determined is denoted as S. Grad corresponds to the gradient from the plot of integrated fluorescence intensity *vs.* absorbance at the excitation wavelength, and η the refractive index of the solvent for the standard and reference.[91,92] As observed from Table 3, the value of QY increased with an increase in the number of thiophene core units. The highest QY was recorded for **T2** with a value of 1.8% and with the lowest recorded for **F2** with 0.014%, as given in Table 3. However, in the series, the thiophene

characteristic and failed to show tautomer emission in all the solvents except THF. The sensitivity of the emission energy due to the changes in solvent polarity was highly evident for all the molecules in the series. Solvent polarity induces a greater charge separation in the excited state, which in turn, provokes a higher dipole moment at the excited state than that in the ground state.[88,89] The normal Stokes shift measured considering the excitation energy and keto emission is roughly 132 nm for **T3** in ACN solvent. The so-called large Stokes shift recorded between the keto emission and enol emission is around 30 nm in the series, and the highest observed for **P2** is 40 nm in DMF solvent.

An enormous amount of work in the literature covers the ESIPT mechanism of molecules in the solvent medium. However, solid state emitters undergoing ESIPT have not been explored much to date. The mechanism supporting excited state proton transfer in the solid state remains unclear.[90] The molecules in the series were deposited onto chemically and ultrasonically cleaned glass substrates *via* vacuum thermal vapor deposition at a base pressure of 5×10^{-6} mbar. Thin films with a thickness of 50 nm were obtained after deposition

Table 2 Photophysical parameters of the molecules in thin film form

	$\lambda_{excitation}$ (nm)	$\lambda_{emission}$ (nm) Keto	Enol	Normal Stokes shift (nm)	Large Stokes shift (nm)	FWHM (nm)
T2	385	451	475	66	24	102
P2	376	463	491	87	28	104
F2	376	459	482	83	23	100
T3	435	504	610	69	106	78
P3	387	494	523	107	29	98
F3	420	690	—	270	—	136

Table 3 The measured quantum yield of all the molecules

Molecule	T2	P2	F2	T3	P3	F3
QY (%)	1.80	0.15	0.014	0.273	0.02	0.08

substituent present on the side chain of the central core gave a better quantum yield in comparison with that for furan and pyridine.

$$\phi_S = \phi_R \left[\frac{\text{Grad}_S}{\text{Grad}_R} \right] \frac{\eta_S^2}{\eta_R^2} \qquad (1)$$

The restriction of the vibrational and rotational components in a system upon aggregation enhances the emission intensity in the solid state over solution. However, the solid-state molecular packing and aggregation type decide the quantum efficiencies of ESIPT chromophores.[90] To better understand the effect of aggregation on the emission intensity of the molecules, AIE studies were performed for the series at different ratios of H$_2$O/THF mixture. Solutions were prepared with a concentration of 10^{-5} M in THF, and their mixtures in varying water fractions f_w were used for AIE studies. Fig. 3 shows the fluorescence emission of the series with different H$_2$O/THF mixtures under UV irradiation of 365 nm. Herein, 10% for f_w implies a 10:90 mixture with 10% of H$_2$O and 90% of THF and 20% for f_w implies 20:80 with 20% of H$_2$O and 80% of THF, and so on. **F3** exhibited good AIE characteristics, as shown in Fig. 4, in contrast with the others in the series, which showed aggregation-caused quenching (ACQ), as shown in [S32–S36, ESI†]. The aggregation of **F3** in a poorer solvent medium resulted in an enhancement in emission intensity and reached the maximum at 80% H$_2$O/THF ratio and then decreased rapidly upon a further increase in f_w. The drop in emission intensity at higher ratios of H$_2$O/THF mixture is due to the poor solubility of the solute in solvent mixture.[93] The polarity of the mixture increases upon an increase in the ratio of f_w, which lowers the energy bandgap in the system, and hence, a redshift was observed at a higher f_w.[94] The redshift is highly predominant in **F3**, and the shift of 45 nm observed in the

Fig. 4 Photographs of the molecules in THF/water mixtures with different f_w under UV illumination.

emission wavelength with an increase in f_w is indicative of positive solvatochromism.[95] On the other hand, **F2** at the initial ratios exhibited an increasing trend in intensity and stabilized to a fixed value with an increase in f_w and decreased at higher f_w ratios. The absence of double peaks at higher ratios of f_w is indicative of the absence of proton transfer in the excited state owing to an increase in the solvent polarity.

Cyclic voltammetry

The electrochemical properties of the molecules were studied by cyclic voltammetry to estimate their electronic energy levels and bandgap. **T2**, **P2**, and **F2** showed a good quasi-reversible oxidation and reduction peak, as shown in Fig. 5; whereas, **T3**, **P3** and **F3** exhibited quasi-irreversible curves, as shown in Fig. 6 with their estimated energy level given in the inset plot. The enhanced conjugation for **T3**, **P3** and **F3** with hydrazides on both arms chemically connected with the thiophene di-aldehyde group hampered the peaks during the reduction cycle. Oxidation peak corresponds to the involvement of the –NH functionality in oxidation and reduction peak corresponds to the –C=O functionality involved in the reduction process of the series. The HOMO and LUMO energy levels and band gap of **T2**, **P2** and **F2** are analogous, and hence the substituted hydrazides on the bi-thiophene moiety had no significant role in altering the energy levels of the molecules. The energy bandgap of all the molecules was estimated using the equation

Fig. 3 Fluorescence emission spectra of **F3** with varying f_w and inset shows the intensity value with varying f_w.
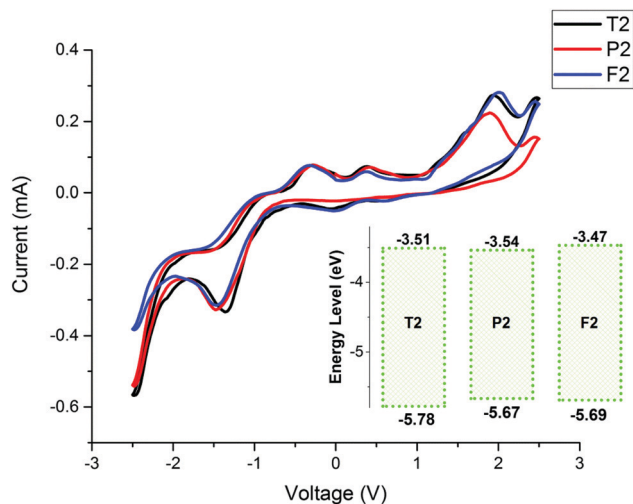
Fig. 5 Cyclic voltammograms of the **T2**, **P2**, and **F2** molecules with their energy levels.
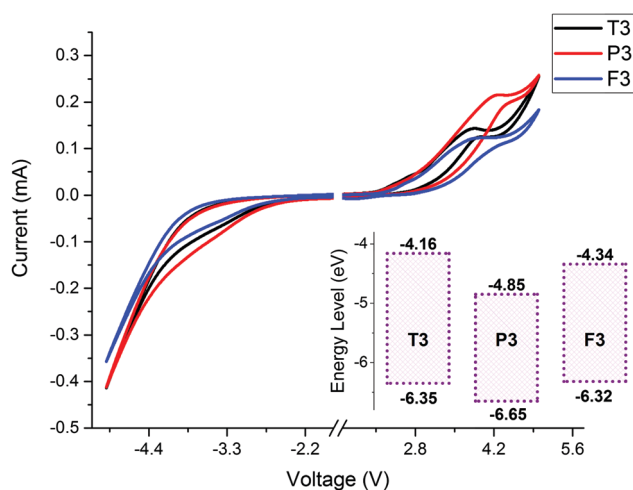

Fig. 6 Cyclic voltammograms for the **T3**, **P3**, and **F3** molecules with their energy levels.

$E_{HOMO} = -(I_p + 4.4)$ eV and LUMO by $E_{LUMO} = -(E_A + 4.4)$ eV,[96] with the results tabulated in Table 4. The HOMO energy level for **T3**, **P3**, and **F3** was obtained from their cyclic voltammograms using the equation mentioned above. The LUMO energy levels of the series were derived from the energy gap of the solid-state photoluminescence spectra and the estimated HOMO level

Table 4 Electrochemical parameters and the electronic energy levels of all the molecules

	I_P (V)	E_A (V)	HOMO (eV)	LUMO (eV)	E_G (eV)
T2	1.38	−0.89	−5.78	−3.51	2.27
P2	1.27	−0.86	−5.67	−3.54	2.13
F2	1.13	−0.93	−5.69	−3.47	2.22
T3	1.95	^{a}	−6.35	−4.16	2.16
P3	2.25	^{a}	−6.65	−4.85	1.80
F3	1.92	^{a}	−6.32	−4.34	1.98

^{a} Reduction not obtained from the cyclic voltammogram.

from the cyclic voltammogram. The HOMO of **T3** and **F3** showed a similar energy value of around ∼−6.3 eV with **T3** having a LUMO level of −4.16 eV and that of **F3** was −4.34 eV. **P3** exhibited a slightly more negative HOMO value of −6.65 eV in comparison with that of **T3** and **F3** and a shallow LUMO level of −4.85 eV. The highest energy bandgap, E_G, obtained in the series was for **T2** with 2.27 eV, and the lowest obtained for **P3** of 1.8 eV.

DFT studies

Fig. 7 shows the possible normal and tautomeric structures of all the molecules, where specifically, **T2**, **P2**, and **F2** can solely support a single proton translocation. The keto form is believed to be the thermodynamically stable structure, which is denoted as k, while the enol form (e) is believed to be the kinetically stable entity, corresponding to the tautomeric form occurring after photoexcitation of the molecules. **T3**, **P3**, and **F3** possessing dual hydrazides may undergo three different possible structures, firstly, both arms exhibiting the keto form (k); secondly, one of the arm exhibiting the keto form and the other exhibiting the enol form, which is represented as (e). The third is the hypothetical tautomeric form, denoted as o, with both arms showing the enol form, which is strictly impossible. Supposing, if such a transformation occurs in a system, the system may mutate to the keto and enol forms across the arms (i.e., the e form), and hence a double enol structure is difficult to realize. Zhang et al. provided proof for the impossible double proton transfer concurrently occurring in a system, despite its structural attributes supporting double proton transfer.[4]

Structures possessing a single substituted hydrazide covalently linked with a single thiophene moiety, which were denoted as **T1**, **P1** and **F1**, were also studied. **T1** and **F1** were designed and synthesized to investigate their practical cation sensing applications.[97] **T1**, **P1**, and **F1** exhibit extremely weak fluorescence emission in solution and the solid state, and hence it is difficult to ascertain their keto–enol transition energies. The theoretical aspects dealing with the excited state dynamics of these molecules have not been reported to date, and are solely discussed herein for comparison with the present study. The computed ground state vibrational spectra of **T1**, **P1**, and **F1** in comparison with their excited state was redshifted by a finite value, as shown in Fig. 8. This redshift indicates the weakening of the intramolecular hydrogen bond in their excited state, and hence confirm a difficult excited state proton translocation. The emission energy transition estimated for the k-form is around ∼340 nm and for the e-form is ∼375 nm. The probability of enolic transition is greater in comparison with that of the keto transition, and hence the oscillator strength of the e-form is higher than that of the k-form. Thus, potential energy scans were attempted to verify any possibility of proton transfer in the excited state. However, repeated attempts failed to estimate the transition structure of these molecules in the excited state. Due to the above-mentioned reasons, we concluded that **T1**, **P1**, and **F1** do not support excited state intramolecular proton transfer.
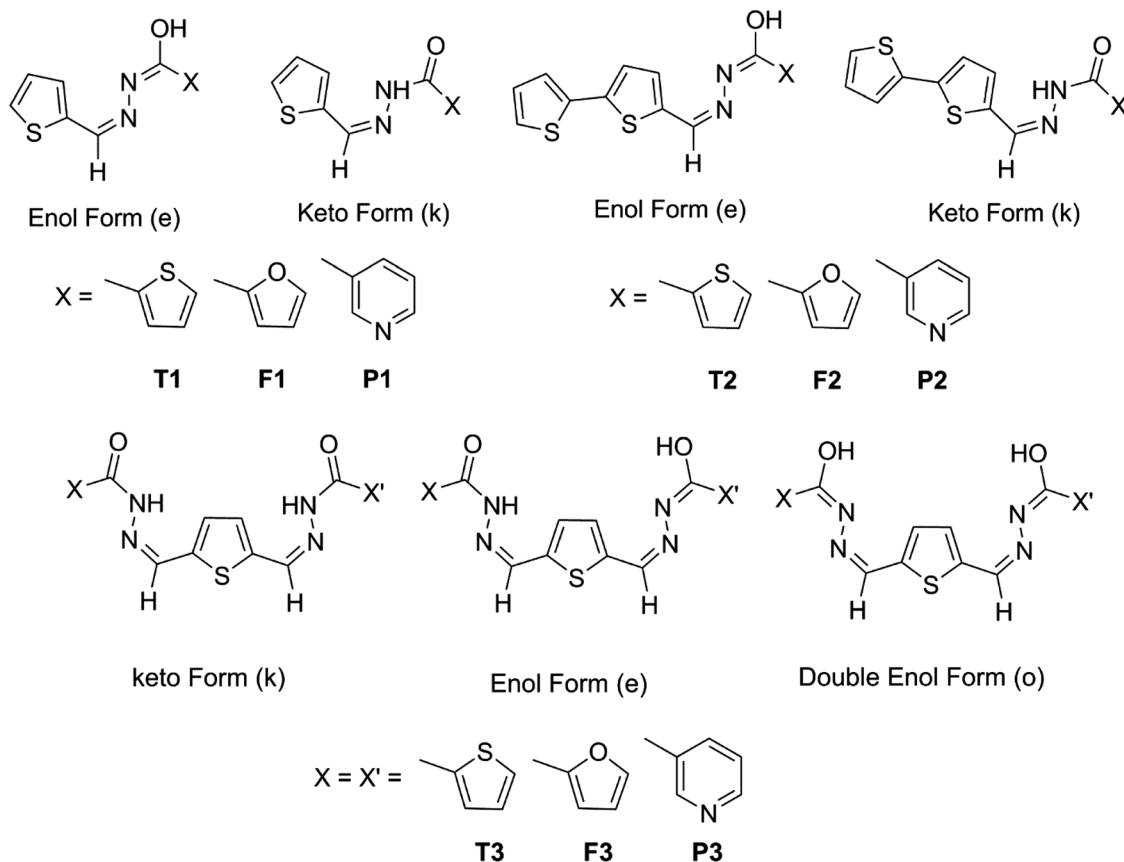
Fig. 7 Probable tautomeric structures of molecules with the keto (k), enol (e) and double enol (o) forms.
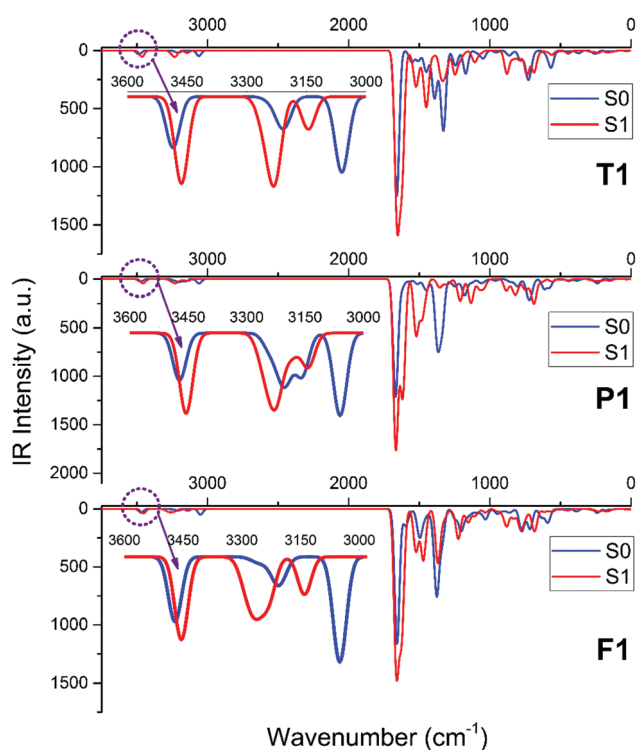

Fig. 8 Vibrational stretching frequency of **T1**, **P1** and **F1** in the S_0 and S_1 states, specifically focusing of the N–H stretching frequency.

Geometry

The ground state geometry optimized normal form (k) of all the structures is shown in Fig. 9 and their structural attributes are summarized in Table 5. The N–H distance of the normal form (k) for all the structures remained unaffected to a value of 1.020 Å in both S_0 and S_1. However, the intramolecular hydrogen bond distance d and d', was shortened at the excited state S_1 in comparison with that of the ground state, S_0. The value of R was reduced from 2.340 Å and 2.378 Å to 2.324 Å and 2.359 Å
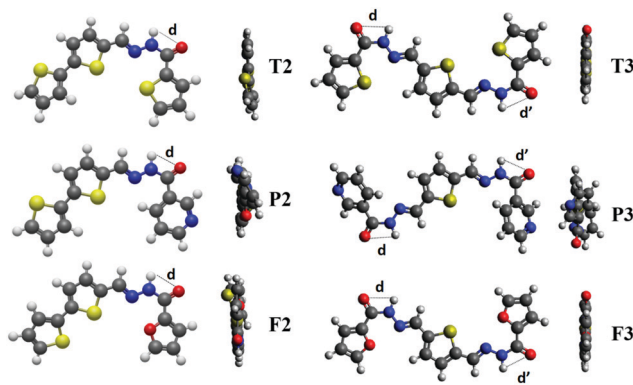

Fig. 9 Intermolecular associations of the molecules of the series with O–H bond distances. Color code: O-atoms, red; C-atoms, grey; N-atoms: blue, and S-atoms, green.

Table 5 Geometrical parameters of the molecules at S_0 and S_1

	N–H distance (Å)		d (Å)		d' (Å)	
	S_0	S_1	S_0	S_1	S_0	S_1
T2	1.019	1.018	2.401	2.401	—	—
P2	1.020	1.020	2.340	2.324	—	—
F2	1.020	1.020	2.378	2.359	—	—
T3	1.019	1.020	2.396	2.377	2.396	2.380
P3	1.020	1.020	2.404	2.369	2.406	2.370
F3	1.019	1.020	2.375	2.353	2.377	2.359

for **P2** and **F2**, respectively, while there was no change observed for **T2** in S_0 and S_1. Similarly, the value of d and d' showed a reduction in the intramolecular hydrogen bonding distance for **T3**, **P3** and **F3** at S_1 in comparison with that at S_0; however, a single proton is expected to translocate from the donor to acceptor. The lowering of the hydrogen bond distance at the excited state, S_1, in comparison with S_0 is highly supportive of possible excited state intramolecular proton transfer.[2,98] Interestingly, **P3** showed a phenomenal reduction in d and d' in comparison to the other five-membered ring in the series. One of the possible reasons is that the effect of a six-membered heterocyclic ring tends to stabilize the structure by gaining greater control over the distance of the H-bonding interaction. **P3** possesses a dihedral angle of 39° at S_0, which is reduced to 32.6° at S_1 between the extended thiophene core and pyridine moiety. The molecules in the series with a bithiophene moiety possess a certain minimal dihedral angle between the bithiophene core, and at their excited state, this angle becomes to zero to support ESIPT in the system. **T2** and **F2** possess a dihedral angle of 19° and 27° between the bithiophene rings at S_0, respectively, which changes to 0.1° at S_1. Structural planarity may better support and ease proton transfer in a system than a non-planar structure.[98]

Spectral quality and frontier molecular orbitals

Molecular orbitals, especially the highest occupied molecular orbitals (HOMO) and lowest unoccupied molecular orbitals (LUMO), play an essential role in governing the overall chemical reactivity of a system.[99] The energy gap between the HOMO and LUMO determines dynamic stability, chemical hardness, and chemical reactivity, and it further provides an overall understanding of the reaction pathway and molecular activity of a complex. The theoretically estimated HOMO and LUMO levels and energy band gap of all the molecules in THF solvent are provided in Fig. 10. The significant contribution of electronic transitions (CI $\sim$93% to 97%) occurring within the system for both the normal form and the tautomeric form is governed by the HOMO and LUMO. Hence, herein, the discussion is restricted to the HOMO and LUMO, which correspond to π–π* orbitals. The energy band gap values of all the molecules lie around $\sim$3.3 eV, except for **T2**, showing a slightly higher value of 3.62 eV. The significant contribution of HOMO and LUMO is from the π orbitals and the core moiety. The theoretical estimation of the energy bandgap for the conjugation-enhanced structure of **T3** and **F3** exhibited a seemingly small

energy reduction in comparison with that for **T2** and **F2**, supporting the experimental results, while, these differences were not distinguishable in **P3**. The HOMO and LUMO of **T2** are completely distributed on its entire molecular network, while, for **T3**, **P3**, and **F3** they are mainly centered on the thiophene and a portion is on the keto moiety. The orbitals of the series exhibited a size reduction in the electron cloud engulfing the proton donor moiety (N–H) in the LUMO level in comparison with that of the HOMO, while there was almost no change in the electron density on the O atom belonging to the carbonyl moiety.[100] These changes in electron density suggest an enhanced interaction between the hydrogen donor and acceptor moiety at the excited state and can better induce alienation of a proton from a donor moiety.[98,101] The effect of intramolecular charge transfer (ICT) is highly evident in **P2** and **F2**, which further helps easy separation of a proton from a donor moiety.[98] Further, upon comparing the HOMO and LUMO electronic distributions of all the systems, it can be seen that the proton acceptor oxygen exhibits a σ-type orbital; whereas, –NH exhibits a π–π*-type distribution. The observed distribution around –NH at the HOMO level clearly indicates the strong electron withdrawing capability of the nitrogen moiety, readily giving up a proton upon photoexcitation from the S_0 to S_1 state.[34]

Analysis of the vibrational stretching frequencies of the proton donor moiety involved in intramolecular hydrogen bonding can provide effective information on the dynamics of hydrogen bonding at the excited state.[2,102–104] The stretching vibrational frequencies of the N–H moiety in S_0 and S_1 were analyzed to predict the ESIPT mechanism occurring in the system. The vibrational spectra revealed that the peak corresponding to the N–H stretching was red-shifted in the excited state in comparison with the ground state, as shown in S32 and Table S1 (ESI†) provides the –NH stretching frequency in the S_0 and S_1 state. Han and co-worker proposed the strengthening of the intramolecular hydrogen bond in the excited state is strongly related to the observed red-shift in the stretching vibrations of the proton donor moiety.[79,105] The redshift observed for the bithiophene series is higher in comparison with that for the thiophene series. This may be attributed to the extended conjugation in the thiophene series, which enhances their influence over hydrogen bonding compared to that for the bithiophene moieties. The higher the red-shift observed in the excited state, the lower the potential energy barrier for efficient proton transfer.[102] The N–H stretching vibration was relaxed in the excited state compared with that of the rigid stretching in the ground state, which is evident from the higher intensity of the N–H stretching vibration in the excited state in comparison with the ground state.

The calculations yielding the six lowest lying singlet vertical excitations and the energy of that transition together with the oscillator strength for all the molecules in the series are reported in Table S2 (ESI†). The electronic transitions associated with the keto absorbance (k abs), keto emission (k emi) and tautomer enol emission (e emi) for all the molecules are presented in Fig. 11, where k abs*, k emi* and e emi* represent the experimental values, respectively. The discrete transition
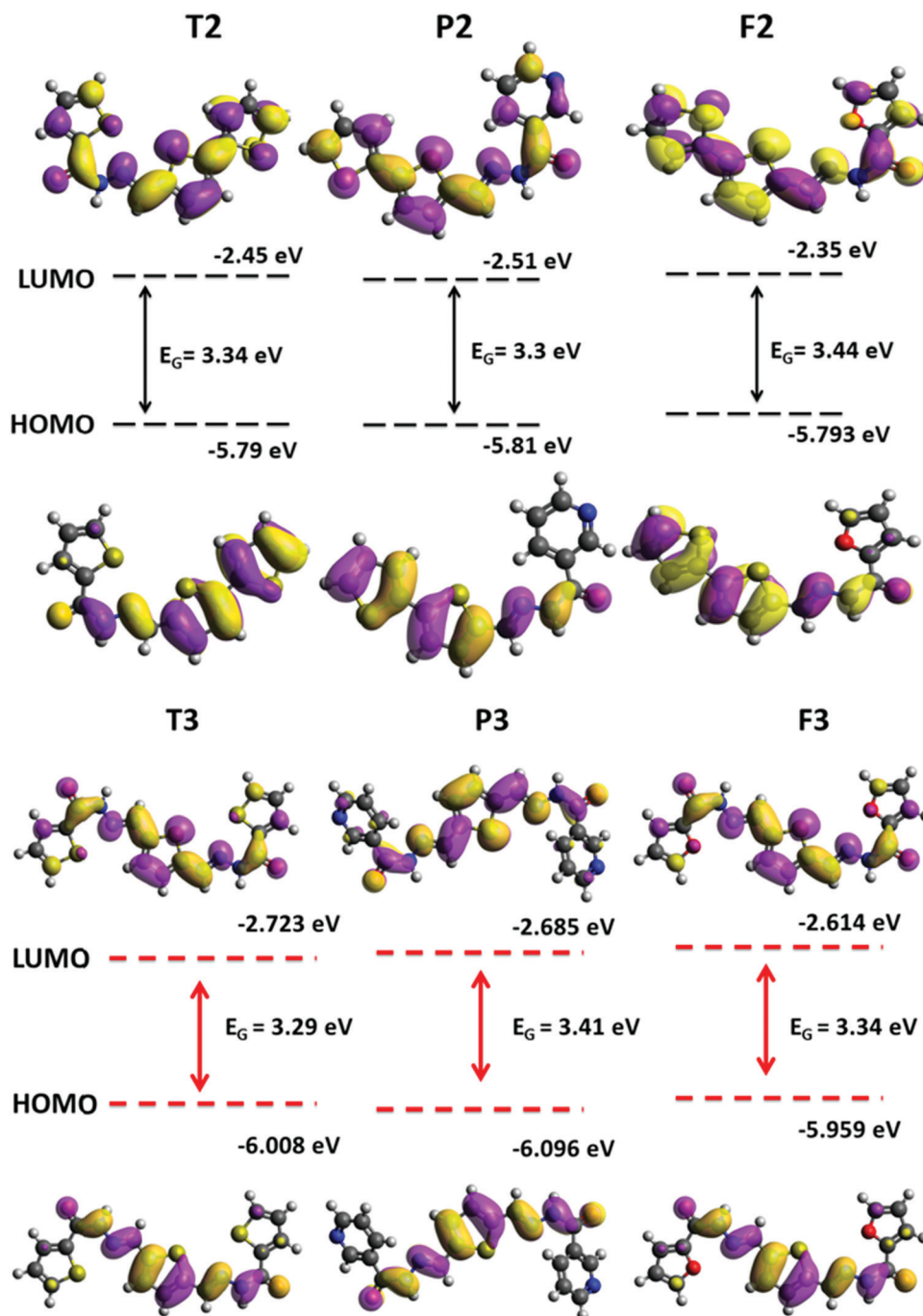
Fig. 10 Electronic orbital representations of all the molecules in the series with their energy levels.

energies obtained after the calculations were broadened by setting the value of FWHM to 50 nm to better accommodate the experimental parameters in the spectra. The results reveal the major transition in the emission spectra occurring in the system is mainly from $S_1 \rightarrow S_0$, suggesting $\pi-\pi^*$ nature. The spectroscopic nature of the absorption spectrum for the k form follows a similar trend to that obtained experimentally, and the absorption peak centered at around 350–370 nm for all the molecules is close to the experimental figures. The emission energy obtained from the k form and e form correlate well with the experimentally observed spectra with a slightly overestimated energy difference of ~0.3 eV.[103,104,106,107] The oscillator strength of the e form estimated theoretically is higher in comparison with that of the k form for a few of the molecules, which is consistent with the experimental evidence. Moreover, it is essential to note that the energy emission of the k form for all the series is higher in energy in comparison to that of e form, establishing the k form as the thermodynamically stable state. The energy difference of the emission spectrum between the k form and the e form of the series is analogous to the experimentally obtained values.
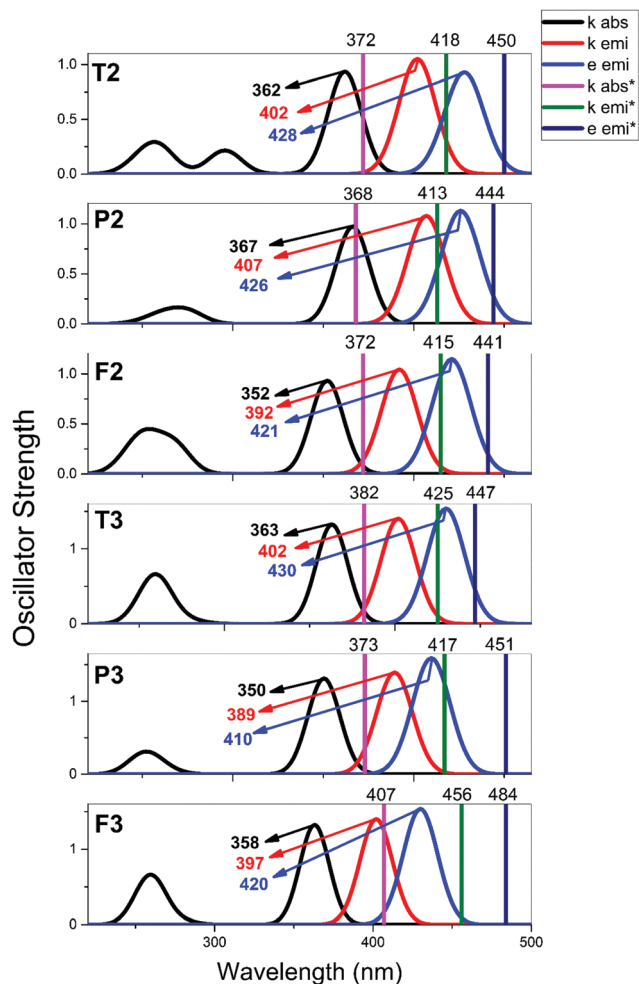
Fig. 11 Experimentally observed and theoretically estimated absorption and emission spectra for the keto and enol forms of all the molecules.

Fig. 12 Single point energies of **T2**, **P2** and **F2** molecules as a function of rotation of the dihedral angle for both S_0 and S_1. Black colored atom: thiophene, furan or pyridine.
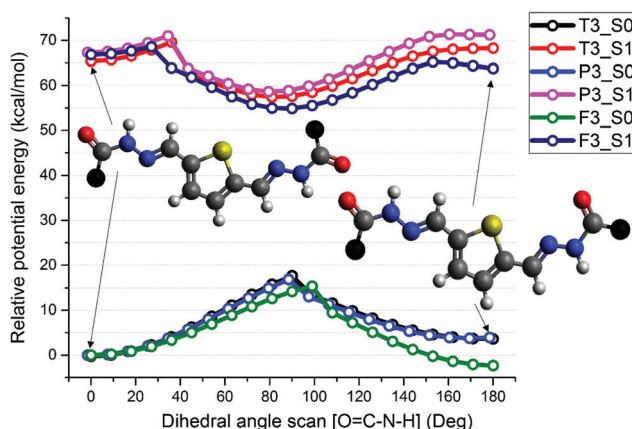
Fig. 13 Single point energies of **T3**, **P3**, and **F3** molecules as a function of rotation of the dihedral angle for both S_0 and S_1. Black colored atom: thiophene, furan or pyridine.

Potential energy curve of ESIPT reactions

Since the molecules in the series support single proton transfer alone in the excited state, the potential energy curves (PECs) for both the ground and the excited state were estimated. The PEC is a useful technique that nurtures the subtleties of molecular properties and gives information about the nature of hydrogen transfer reactions along the proton transfer path. The PEC was simulated using the B3LYP functional with the 6-31G basis set for a complete rotation of $0°–180°$ between the carbonyl and –NH group. The variation in potential energy as a function of dihedral angle for all the molecules is provided in Fig. 12 and 13. The optimized structures with zero dihedral angles between the plane connecting –NH and –C=O seem to be energetically more stable than that with a dihedral angle of $180°$, as evident from the values at the extremities of the curve. The results show that **F3** tends to acquire a geometry that does not favor optimal intramolecular hydrogen bonding between the donor and acceptor moieties, which hinders ESIPT in comparison with the other types.

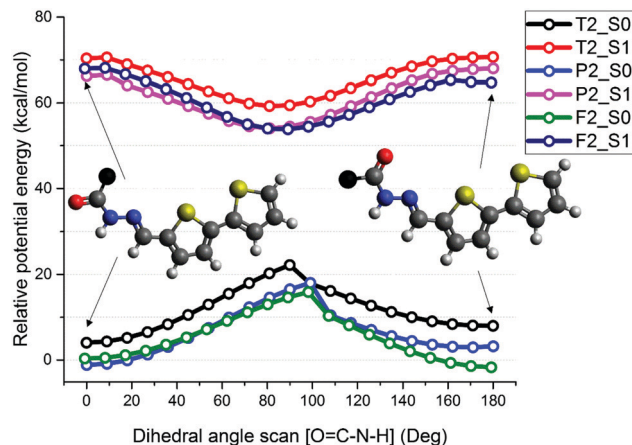The potential energy scans were acquired on the constrained optimized geometry at the corresponding electronic states with a fixed O–H bond length. The consistency in the reproduction of the results by DFT with the experimental results may not be precise; however, previous calculations proved to be effective in providing qualitative results for accurate pathways supporting proton transfer.[84,108–110] The potential energy curve of molecule **T2** is provided in Fig. 14 and that for the rest of the molecules is provided in S38–S42 (ESI†), where the term FB indicates forward barrier and the RB indicates the reverse barrier for both the S_0 and S_1 states. FB refers to the difference between the stable keto state and the point at which the potential reaches the maximum along the proton transfer pathway. Similarly, RB refers to the difference between the maximum potential and the stable enol tautomer along the proton transfer pathway. Estimation of the transition structure for **F3** on the potential energy curve at the excited state was difficult to realize. The molecules in the series in their ground state prefer the keto form, and upon excitation changes to the tautomer e-form undergoing ESIPT. The scans pertaining to proton transfer were estimated using DFT to realize the FB and RB
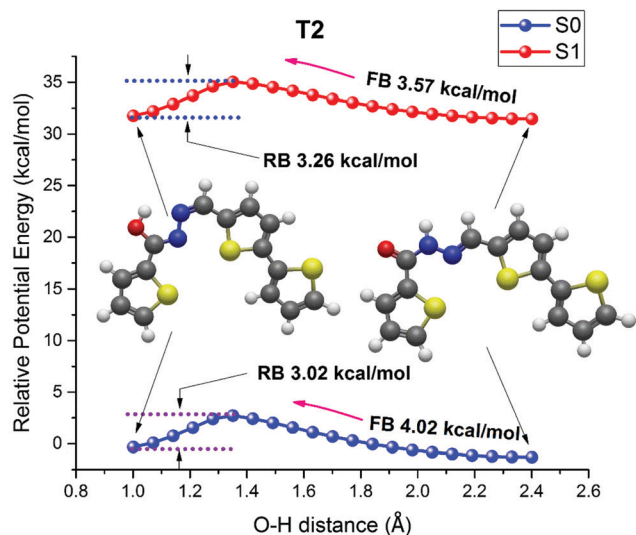
Fig. 14 Single point energies of **T2** molecule in the S_0 and S_1 states calculated using B3LYP and CAM-B3LYP.

potential in both the S_0 and S_1 states. The results illustrate that the FB for all the molecules in the series in their excited state was comparatively less in magnitude than that in the ground state. The lower FB at their respective excited state indicates possible proton transfer at S_1 in comparison with S_0. On average, $\sim$3.57 to $\sim$3.78 kcal mol^{-1} of energy barrier is required for a molecule to undergo ESIPT to adopt a tautomer form. The reverse barrier at the ground state for all the molecules is lower in energy in comparison with that of the FB, which reveals the possible ground state intramolecular proton transfer (GSIPT). **T3** showed a RB higher to FB in its S_0, which may account for the stringent GSIPT. Further, we summarized the whole ESIPT mechanism for the present system with –C=O acting as the proton acceptor and –NH acting as the proton donor. Initially, –C=O is capable of capturing a proton from the nearest –NH donor and forms an intramolecular hydrogen bond in the ground state. Upon photo-excitation, the intramolecular hydrogen bond is strengthened, and a proton translocates from –NH to the –C=O group through a significant forward energy barrier. At an approximate O–H distance of 1.35 Å, the system exhibits the maximum potential energy, and beyond this point, the energy minimizes, and the system possesses the desirable tautomeric structure. The tautomeric structure at S_1 undergoes a spontaneous emission, which is either radiative or non-radiative, to reach its ground state S_0 and reverts to the normal form by crossing a significant RB potential.

PES scans were performed on the system to verify the possibility of double proton translocation arising due to the presence of substituted hydrazides present on both the arms of the thiophene core. The potential energy scans were performed using the DFT-B3LYP functional with the 6-31G basis set for the ground state and CAM-B3LYP with the same basis set for the excited state. The selection of the function is expected to estimate qualitative energetic pathways for the ESIPT

process.[81,90,111–113] The potential energy surface of **T3** and **P3** for both the ground and excited state is provided in Fig. 15 and 16, with the inset providing the surface contour profile. A high amount of symmetry exists on the surface along the diagonal line connecting the ends of the normal and double enol form. It is important to note that the potential energy surface remains the same irrespective of the change in the heteroatom present in the ring. Four minima exist on the PES surface, which are related to the k-form, e-form and o-form, where the estimated potential energy follows the order of $E_k < E_e < E_o$, signifying GSIPT is an endothermic process. A very high potential barrier of value $\sim$8 kcal mol^{-1} exists for the molecules at S_0 and S_1 traced along the path (a → d). This high potential barrier exhibited by the system validates the impossible simultaneous double proton transfer at the excited state. The system after photoexcitation induces a proton to translocate from the proton donor to the proton acceptor species guided along the path (a → c) or (a → b) with a minimal potential energy barrier, attaining the tautomer e-from. A second proton transfer or stepwise double proton transfer can occur if the system gets much higher external energy to overcome the significant barrier potential of $\sim$4.2 kcal mol^{-1} along the path (c → e) or (b → e). The higher barrier potential traversed along the path (c → e) or (b → e) does not support the second proton transfer, thus hindering the step-wise double proton transfer kinetically. Further, supposing a step-wise double proton transfer occurs in the system (a → b → e or a → c → e), the reverse barrier of $\sim$2.8 kcal mol^{-1} from (e → c) or (e → b) is significantly less compared to the forward barrier and the system quickly achieves the e-form. Based on the above discussion, we conclude that the system with hetero-substituted hydrazides support single proton transfer in its excited state and an impossible double proton transfer or step-wise double proton transfer.

Device fabrication and characterization

In the series, **T2** exhibited a good quantum yield of value 1.8%, and the energy levels determined from cyclic voltammetry signifies that **T2**, **P2**, and **F2** can function as emitter materials for organic light emitting diode applications in comparison to **T3**, **P3** and **F3**, which possess a high HOMO level. To evaluate the electroluminescence performances of the synthesized materials, non-doped OLEDs were fabricated with the device structure: ITO/ N,N'-bis(3-methylphenyl)-N,N'-diphenylbenzidine [TPD] (40 nm)/**T2** or **P2** or **F2** (60 nm)/4,4′-bis(N-carbazolyl)-1,1′-biphenyl [CBP] (6 nm)/ tris(8-hydroxyquinolinato)aluminum [Alq$_3$] (35 nm)/lithium fluoride [LiF] (1 nm)/aluminium (150 nm), as shown in Fig. 17. The adopted device architecture is well reported to result in good charge injection and recombination at the emitter material.[114] TPD acts as a hole-injection and hole-transport layer, CBP acts as a hole blocking layer, Alq$_3$ acts as an electron transport layer and aluminium was used as the cathode material. Fig. 18 shows the voltage *vs.* current density plots for the devices with **T2** and **P2** as emitters, with the inset showing the electroluminescence and device emission. As observed, the device required a very high turn-on voltage of $\sim$15 V for initiating electroluminescence. The voltage *vs.* luminous flux for **T2** and **P2** is shown in Fig. 19, where it can
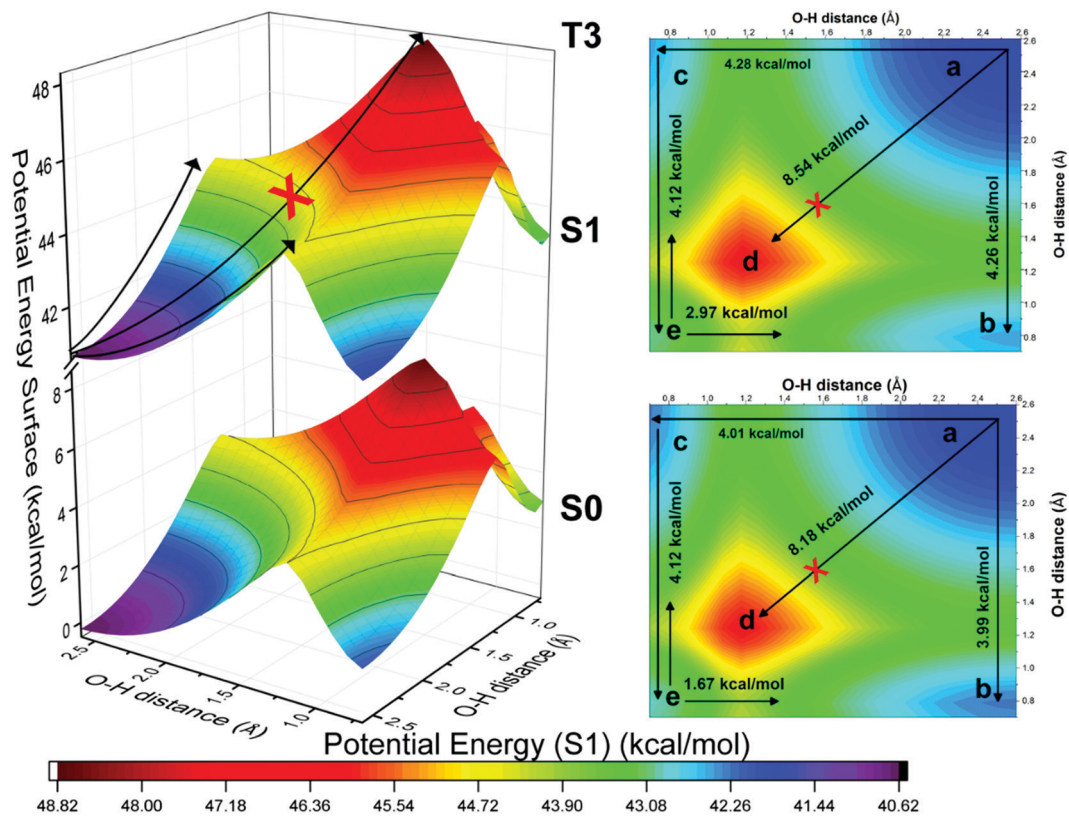
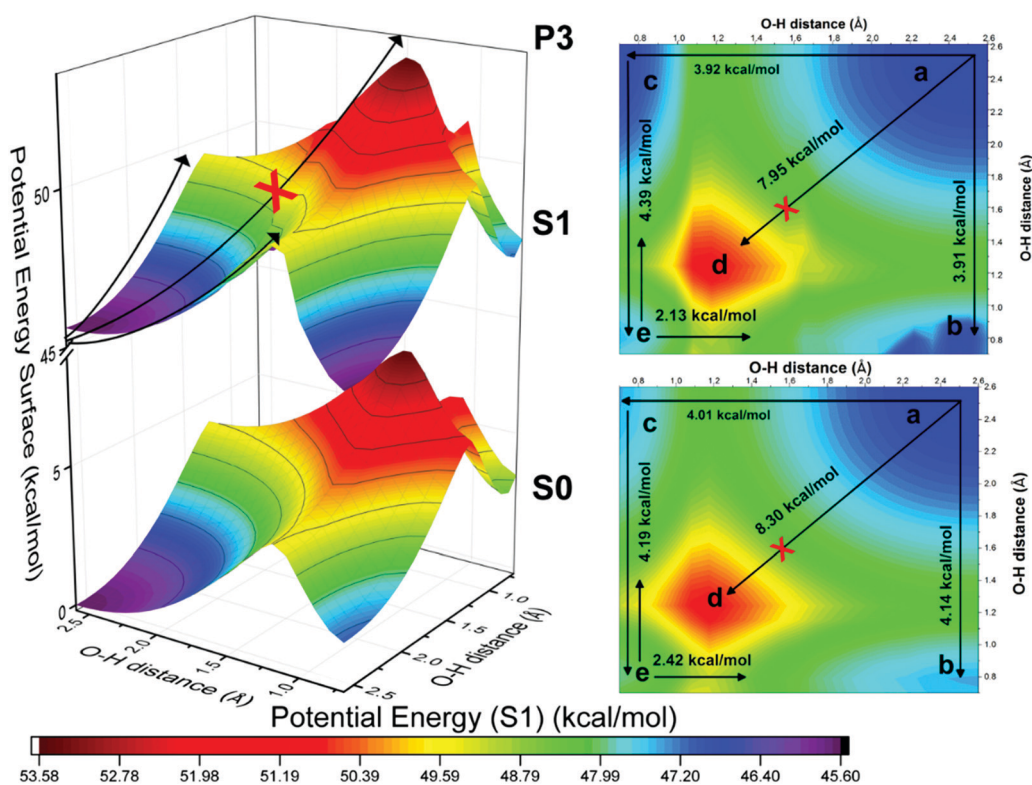**Fig. 15** PES scan of **T3** in the S_0 and S_1 states with their contour profile.

Fig. 16 PES scan of **P3** in the S_0 and S_1 states with their contour profile.
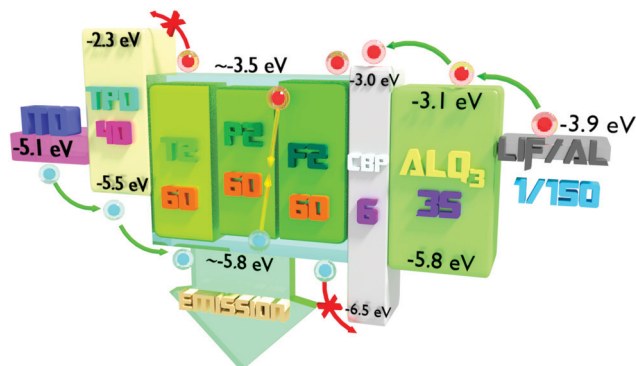
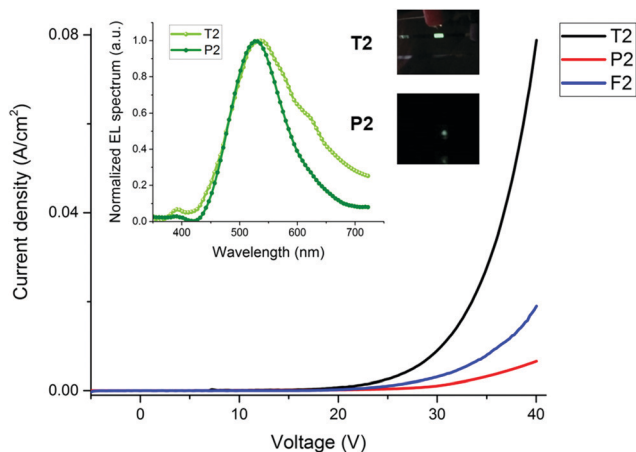**Fig. 17** Device architecture for **T2**, **P2**, and **F2** molecules as an emitter layer.

Fig. 18 $J-V$ characteristics of the device with **T2**, **P2**, and **F2** as the emitter material. Inset showing the EL spectrum and image showing the light emission from the device.
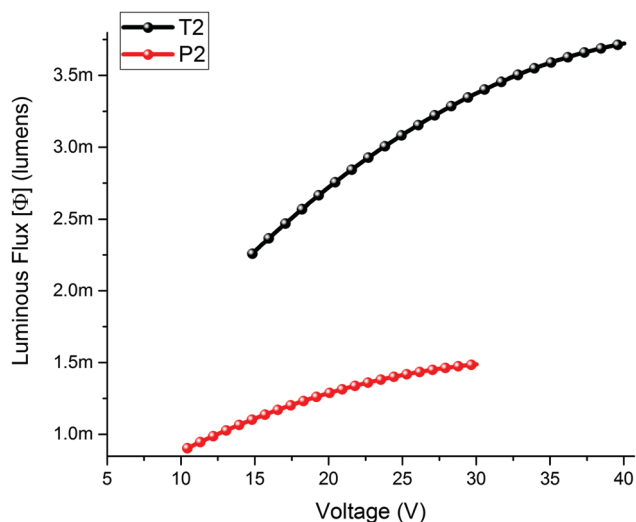

Fig. 19 Voltage luminous flux characteristics of **T2** and **P2** molecules.

be observed that the device exhibited a maximum luminous flux of value 0.035 and 0.015 lumens for **T2** and **P2**, respectively.
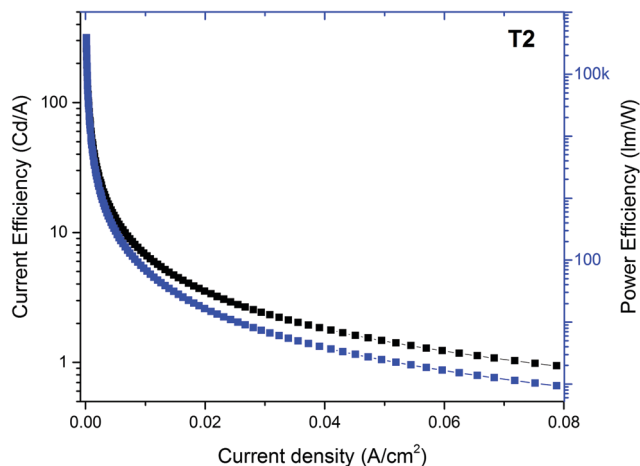

Fig. 20 Current efficiency and power efficiencies of the device with **T2** as an emitter layer.
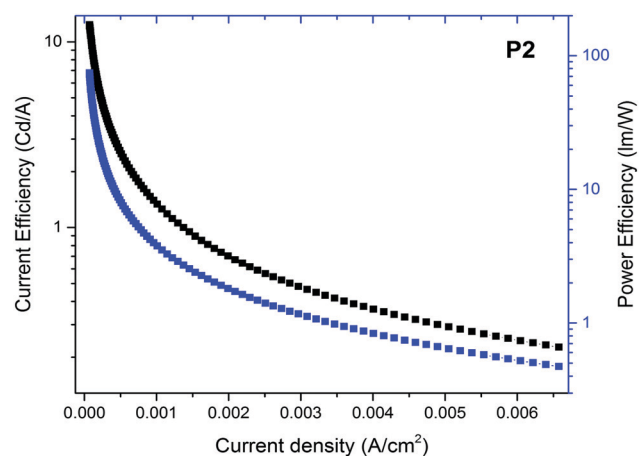

Fig. 21 Current efficiency and power efficiencies of the device with **P2** as an emitter layer.

However, **F2** possessing the lowest quantum yield in the series failed to produce any light. The current efficiency of 0.94 Cd A^{-1} and power efficiency of 0.94 lm W^{-1} were exhibited by the **T2** molecule while **P2** exhibited a current efficiency of 0.23 Cd A^{-1} and power efficiency of 0.18 lm W^{-1}, as shown in Fig. 20 and 21, respectively.

Conclusions

Six heterocyclic substituted hydrazides were designed and synthesized, which initiate intramolecular excited state proton translocation. Their photophysical characterization in solvents of varying dielectric constants signifies the occurrence of a double peak, which correlates to keto and enol transitions. The molecules in the series exhibited good ESIPT in solvents of lower dielectric constants, and thus exhibited a distinct double peak in THF solvent. The AIE studies revealed the molecules without the furan moiety have their emission intensity

quenched upon aggregation. **F3** possessing furoic hydrazide exhibited a good AIE effect and failed to support ESIPT in the solid state. **T2** exhibited the highest quantum yield of 1.8% in the series, which decreased upon aggregation. The cyclic voltammetry study revealed bithiophene covalently linked with substituted hydrazide possesses an energetically favorable HOMO–LUMO level for efficient device application. OLEDs were realized using **T2** and **P2** as emitter materials embedded in the device architecture of ITO/TPD/**T2** or **P2**/CBP/Alq$_3$/LiF/Al. The current efficiency of 0.94 Cd A^{-1} and 0.23 Cd A^{-1} for **T2** and **P2** together with the power efficiency value of 0.94 lm W^{-1} and 0.18 lm W^{-1} were obtained, respectively. The energy-optimized ground state geometry of all the tautomers and their electronic orbital distribution well support the excited state intramolecular proton transfer phenomenon. The theoretically derived vibrational spectra of **T1**, **P1** and **F1** did not favor ESIPT. However, the conjugation-enhanced structure in the synthesized molecules supports ESIPT. The theoretical energy transitions of the keto–enol tautomer well correlate with the pertinent energy transitions experimentally observed. The potential energy scans performed on the molecules revealed the existence of a lower forward barrier in their excited state in comparison with their ground state, suggesting excited-state proton translocation. Also, the potential energy surface scan performed on **T3**, **P3** and **F3** confirm the impossible double proton transfer and difficult step-wise double proton transfer.

Conflicts of interest

There are no conflicts of interest to declare.

Acknowledgements

References

1 J. M. Mir, S. Roy, P. K. Vishwakarma and R. C. Maurya, *J. Chin. Adv. Mater. Soc.*, 2018, **6**, 282–300.

2 J. Zhao, J. Chen, Y. Cui, J. Wang, L. Xia, Y. Dai, P. Song and F. Ma, *Phys. Chem. Chem. Phys.*, 2015, **17**, 1142–1150.

3 J. Zhao, X. Liu and Y. Zheng, *J. Phys. Chem. A*, 2017, **121**, 4002–4008.

4 M. Zhang, Q. Zhou, C. Du, Y. Ding and P. Song, *RSC Adv.*, 2016, **6**, 59389–59394.

5 J. Zhao, J. Chen, J. Liu and M. R. Hoffmann, *Phys. Chem. Chem. Phys.*, 2015, **17**, 11990–11999.

6 J. Zhao, H. Dong and Y. Zheng, *J. Lumin.*, 2018, **195**, 228–233.

7 G.-Y. Li and K.-L. Han, *Wiley Interdiscip. Rev.: Comput. Mol. Sci.*, 2018, **8**, e1351.

8 P. F. Barbara, P. M. Rentzepis and L. E. Brus, *J. Am. Chem. Soc.*, 1980, **102**, 2786–2791.

9 P. F. Barbara, L. E. Brus and P. M. Rentzepis, *J. Am. Chem. Soc.*, 1980, **102**, 5631–5635.

10 J. Zhao, H. Dong and Y. Zheng, *J. Phys. Chem. A*, 2018, **122**, 1200–1208.

11 J. Zhao, H. Dong, H. Yang and Y. Zheng, *Org. Chem. Front.*, 2018, **5**, 2710–2718.

12 A. Weller, *Z. Elektrochem.*, 1956, **60**, 1144–1147.

13 A. L. Sobolewski, W. Domcke and C. Hättig, *J. Phys. Chem. A*, 2006, **110**, 6301–6306.

14 M. F. Rode and A. L. Sobolewski, *J. Phys. Chem. A*, 2010, **114**, 11879–11889.

15 S. Mahanta, B. K. Paul, R. B. Singh and N. Guchhait, *J. Comput. Chem.*, 2011, **32**, 1–14.

16 J. Zhao, S. Ji, Y. Chen, H. Guo and P. Yang, *Phys. Chem. Chem. Phys.*, 2012, **14**, 8803–8817.

17 S. Park, J. E. Kwon and S. Y. Park, *Phys. Chem. Chem. Phys.*, 2012, **14**, 8878–8884.

18 N. Singla and P. Chowdhury, *Chem. Phys. Lett.*, 2012, **548**, 71–79.

19 S. Hayaki, Y. Kimura and H. Sato, *J. Phys. Chem. B*, 2013, **117**, 6759–6767.

20 J. Jankowska, M. F. Rode, J. Sadlej and A. L. Sobolewski, *ChemPhysChem*, 2014, **15**, 1643–1652.

21 W. Yang and X. Chen, *Phys. Chem. Chem. Phys.*, 2014, **16**, 4242–4250.

22 H. Roohi, F. Hejazi, N. Mohtamedifar and M. Jahantab, *Spectrochim. Acta, Part A*, 2014, **118**, 228–238.

23 A. J. Stasyuk, M. K. Cyrański, D. T. Gryko and M. Solà, *J. Chem. Theory Comput.*, 2015, **11**, 1046–1054.

24 S.-H. Xia, B.-B. Xie, Q. Fang, G. Cui and W. Thiel, *Phys. Chem. Chem. Phys.*, 2015, **17**, 9687–9697.

25 Y. Li, L. Wang, X. Guo and J. Zhang, *J. Comput. Chem.*, 2015, **36**, 2374–2380.

26 Y. Houari, S. Chibani, D. Jacquemin and A. D. Laurent, *J. Phys. Chem. B*, 2015, **119**, 2180–2192.

27 L. Gutiérrez-Arzaluz, F. Cortés-Guzmán, T. Rocha-Rinza and J. Peón, *Phys. Chem. Chem. Phys.*, 2015, **17**, 31608–31612.

28 J. Cheng, D. Liu, W. Li, L. Bao and K. Han, *J. Phys. Chem. C*, 2015, **119**, 4242–4251.

29 G. A. Parada, T. F. Markle, S. D. Glover, L. Hammarström, S. Ott and B. Zietz, *Chem. – Eur. J.*, 2015, **21**, 6362–6366.

30 C. Li, C. Ma, D. Li and Y. Liu, *J. Lumin.*, 2016, **172**, 29–33.

31 K. Sakai, S. Tsuchiya, T. Kikuchi and T. Akutagawa, *J. Mater. Chem. C*, 2016, **4**, 2011–2016.

32 G.-J. Zhao and K.-L. Han, *Acc. Chem. Res.*, 2012, **45**, 404–413.

33 J. Zhao, H. Yao, J. Liu and M. R. Hoffmann, *J. Phys. Chem. A*, 2015, **119**, 681–688.

34 J. Zhao, X. Liu and Y. Zheng, *J. Lumin.*, 2017, **188**, 1–6.

35 K.-C. Tang, M.-J. Chang, T.-Y. Lin, H.-A. Pan, T.-C. Fang, K.-Y. Chen, W.-Y. Hung, Y.-H. Hsu and P.-T. Chou, *J. Am. Chem. Soc.*, 2011, **133**, 17738–17745.

36 P. S. Sherin, J. Grilj, Y. P. Tsentalovich and E. Vauthey, *J. Phys. Chem. B*, 2009, **113**, 4953–4962.

37 L. Pinto da Silva, P. J. O. Ferreira, D. J. R. Duarte, M. S. Miranda and J. C. G. Esteves da Silva, *J. Phys. Chem. A*, 2014, **118**, 1511–1518.

38 F. J. Aparicio, M. Holgado, A. Borras, I. Blaszczyk-Lezak, A. Griol, C. A. Barrios, R. Casquel, F. J. Sanza, H. Sohlström, M. Antelius, A. R. González-Elipe and A. Barranco, *Adv. Mater.*, 2011, **23**, 761–765.

39 S. Chen, P. Hou, J. Wang and X. Song, *RSC Adv.*, 2012, **2**, 10869–10873.

40 Z. Song, R. T. K. Kwok, E. Zhao, Z. He, Y. Hong, J. W. Y. Lam, B. Liu and B. Z. Tang, *ACS Appl. Mater. Interfaces*, 2014, **6**, 17245–17254.

41 M. Lan, J. Wu, W. Liu, H. Zhang, W. Zhang, X. Zhuang and P. Wang, *Sens. Actuators, B*, 2011, **156**, 332–337.

42 Z. Xu, L. Xu, J. Zhou, Y. Xu, W. Zhu and X. Qian, *Chem. Commun.*, 2012, **48**, 10871–10873.

43 T.-I. Kim, H. J. Kang, G. Han, S. J. Chung and Y. Kim, *Chem. Commun.*, 2009, 5895–5897.

44 N. Singh, N. Kaur, R. C. Mulrooney and J. F. Callan, *Tetrahedron Lett.*, 2008, **49**, 6690–6692.

45 X.-F. Yang, H. Qi, L. Wang, Z. Su and G. Wang, *Talanta*, 2009, **80**, 92–97.

46 B. Gu, L. Huang, N. Mi, P. Yin, Y. Zhang, X. Tu, X. Luo, S. Luo and S. Yao, *Analyst*, 2015, **140**, 2778–2784.

47 S. Samanta, U. Manna and G. Das, *New J. Chem.*, 2017, **41**, 1064–1072.

48 L. Peng, M. Gao, X. Cai, R. Zhang, K. Li, G. Feng, A. Tong and B. Liu, *J. Mater. Chem. B*, 2015, **3**, 9168–9172.

49 P. Zhang, X. Nie, M. Gao, F. Zeng, A. Qin, S. Wu and B. Zhong Tang, *Mater. Chem. Front.*, 2017, **1**, 838–845.

50 J. Qin, B. Wang, Z. Yang and K. Yu, *Sens. Actuators, B*, 2016, **224**, 892–898.

51 A. I. Ciuciu, L. Flamigni, K. Skonieczny and D. T. Gryko, *Phys. Chem. Chem. Phys.*, 2013, **15**, 16907–16916.

52 Q.-C. Yao, X.-L. Lu and M. Xia, *New J. Chem.*, 2014, **38**, 2693–2700.

53 L. Chen, D. Wu, C. S. Lim, D. Kim, S.-J. Nam, W. Lee, G. Kim, H. M. Kim and J. Yoon, *Chem. Commun.*, 2017, **53**, 4791–4794.

54 D.-E. Wu, Q.-C. Yao and M. Xia, *Phys. Chem. Chem. Phys.*, 2015, **17**, 3287–3294.

55 L. McDonald, J. Wang, N. Alexander, H. Li, T. Liu and Y. Pang, *J. Phys. Chem. B*, 2016, **120**, 766–772.

56 A. Maity, F. Ali, H. Agarwalla, B. Anothumakkool and A. Das, *Chem. Commun.*, 2015, **51**, 2130–2133.

57 L. Peng, S. Xu, X. Zheng, X. Cheng, R. Zhang, J. Liu, B. Liu and A. Tong, *Anal. Chem.*, 2017, **89**, 3162–3168.

58 P. Singh, H. Singh, R. Sharma, G. Bhargava and S. Kumar, *J. Mater. Chem. C*, 2016, **4**, 11180–11189.

59 J. E. Kwon and S. Y. Park, *Adv. Mater.*, 2011, **23**, 3615–3642.

60 H. Liu, X. Cheng, H. Zhang, Y. Wang, H. Zhang and S. Yamaguchi, *Chem. Commun.*, 2017, **53**, 7832–7835.

61 A. Kundu, P. S. Hariharan, K. Prabakaran, D. Moon and S. P. Anthony, *Cryst. Growth Des.*, 2016, **16**, 3400–3408.

62 S. H. Kim, S. Park, J. E. Kwon and S. Y. Park, *Adv. Funct. Mater.*, 2011, **21**, 644–651.

63 Y. Lin, H. Fan, Y. Li and X. Zhan, *Adv. Mater.*, 2012, **24**, 3081.

64 S. C. Rasmussen, K. Ogawa and S. D. Rothstein, *Handbook of Organic Electronics and Photonics*, American Scientific Publishers, Stevenson, Ranch, CA, 2008, vol. 1.

65 M. Granström, M. G. Harrison and R. H. Friend, *Handbook of Oligo- and Polythiophene*, Wiley-VCH, New York, 1999, ch. 8.

66 M. Frisch, G. Trucks, H. Schlegel, G. Scuseria, M. Robb, J. Cheeseman, G. Scalmani, V. Barone, B. Mennucci, G. Petersson, H. Nakatsuji, M. Caricato, X. Li, H. Hratchian, A. Izmaylov, J. Bloino, G. Zheng, J. Sonnenberg, M. Hada, M. Ehara, K. Toyota, R. Fukuda, J. Hasegawa, M. Ishida, T. Nakajima, Y. Honda, O. Kitao, H. Nakai, T. Vreven, J. Montgomery, J. Peralta, F. Ogliaro, M. Bearpark, J. Heyd, E. Brothers, K. Kudin, V. Staroverov, R. Kobayashi, J. Normand, K. Raghavachari, A. Rendell, J. Burant, S. Iyengar, J. Tomasi, M. Cossi, N. Rega, J. Millam, M. Klene, J. Knox, J. Cross, V. Bakken, C. Adamo, J. Jaramillo, R. Gomperts, R. Stratmann, O. Yazyev, A. Austin, R. Cammi, C. Pomelli, J. Ochterski, R. Martin, K. Morokuma, V. Zakrzewski, G. Voth, P. Salvador, J. Dannenberg, S. Dapprich, A. Daniels, O. Farkas, J. Foresman, J. Ortiz, J. Cioslowski and D. Fox, *Gaussian 09, Revision B.01*, Gaussian, Inc., Wallingford CT.

67 C. Lee, W. Yang and R. G. Parr, *Phys. Rev. B: Condens. Matter Mater. Phys.*, 1988, **37**, 785–789.

68 B. Miehlich, A. Savin, H. Stoll and H. Preuss, *Chem. Phys. Lett.*, 1989, **157**, 200–206.

69 P. C. Hariharan and J. A. Pople, *Theor. Chim. Acta*, 1973, **28**, 213–222.

70 W. J. Hehre, R. Ditchfield and J. A. Pople, *J. Chem. Phys.*, 1972, **56**, 2257–2261.

71 T. Yanai, D. P. Tew and N. C. Handy, *Chem. Phys. Lett.*, 2004, **393**, 51–57.

72 J. Tomasi and M. Persico, *Chem. Rev.*, 1994, **94**, 2027–2094.

73 S. Miertus and J. Tomasi, *Chem. Phys.*, 1982, **65**, 239–245.

74 S. Miertuš, E. Scrocco and J. Tomasi, *Chem. Phys.*, 1981, **55**, 117–129.

75 B. Mennucci, E. Cancès and J. Tomasi, *J. Phys. Chem. B*, 1997, **101**, 10506–10517.

76 E. Cancès, B. Mennucci and J. Tomasi, *J. Chem. Phys.*, 1997, **107**, 3032–3041.

77 R. Cammi and J. Tomasi, *J. Comput. Chem.*, 1995, **16**, 1449–1458.

78 Q. Wei, Q. Zhou, M. Zhao, M. Zhang and P. Song, *J. Lumin.*, 2017, **183**, 7–12.

79 G.-J. Zhao and K.-L. Han, *ChemPhysChem*, 2008, **9**, 1842–1846.

80 B. An, H. Yuan, Q. Zhu, Y. Li, X. Guo and J. Zhang, *Spectrochim. Acta, Part A*, 2017, **175**, 36–42.

81 X. Liu, J. Zhao and Y. Zheng, *RSC Adv.*, 2017, 7, 51318–51323.

82 M. D. Hanwell, D. E. Curtis, D. C. Lonie, T. Vandermeersch, E. Zurek and G. R. Hutchison, *J. Cheminf.*, 2012, **4**, 17.

83 R. M. Issa, A. M. Khedr and H. F. Rizk, *Spectrochim. Acta, Part A*, 2005, **62**, 621–629.

84 P. Song and F.-C. Ma, *Int. Rev. Phys. Chem.*, 2013, **32**, 589–609.

85 M. Kasha, *J. Chem. Soc., Faraday Trans. 2*, 1986, **82**, 2379–2392.

86 Hydrogen bonding: a mechanism for tuning electronic and optical properties of hybrid organic–inorganic frameworks | npj Computational Materials, https://www.nature.com/articles/npjcompumats201635, (accessed August 29, 2018).

87 J. Brunel, O. Mongin, A. Jutand, I. Ledoux, J. Zyss and M. Blanchard-Desce, *Chem. Mater.*, 2003, **15**, 4139–4148.

88 B. Liu, Q. Zhang, H. Ding, G. Hu, Y. Du, C. Wang, J. Wu, S. Li, H. Zhou, J. Yang and Y. Tian, *Dyes Pigm.*, 2012, **95**, 149–160.

89 B. Wang, Y. Wang, J. Hua, Y. Jiang, J. Huang, S. Qian and H. Tian, *Chemistry – A European Journal*, 2011, **17**, 2647–2655.

90 V. S. Padalkar and S. Seki, *Chem. Soc. Rev.*, 2015, **45**, 169–202.

91 S. Dhami, A. J. De Mello, G. Rumbles, S. M. Bishop, D. Phillips and A. Beeby, *Photochem. Photobiol.*, 1995, **61**, 341–346.

92 A. T. R. Williams, S. A. Winfield and J. N. Miller, *Analyst*, 1983, **108**, 1067–1071.

93 W. Zhang, N. Wang, Y. Yu, Y.-M. Shan, B. Wang, X.-M. Pu and X.-Q. Yu, *Chem. – Eur. J.*, 2018, **24**(19), 4871–4878.

94 R. Hu, E. Lager, A. Aguilar-Aguilar, J. Liu, J. W. Y. Lam, H. H. Y. Sung, I. D. Williams, Y. Zhong, K. S. Wong, E. Peña-Cabrera and B. Z. Tang, *J. Phys. Chem. C*, 2009, **113**, 15845–15853.

95 Q. Zhang, L. Luo, H. Xu, Z. Hu, C. Brommesson, J. Wu, Z. Sun, Y. Tian and K. Uvdal, *New J. Chem.*, 2016, **40**, 3456–3463.

96 M.-M. Duvenhage, M. Ntwaeaborwa, H. G. Visser, P. J. Swarts, J. C. Swarts and H. C. Swart, *Opt. Mater.*, 2015, **42**, 193–198.

97 V. Tekuri and D. R. Trivedi, *Anal. Chim. Acta*, 2017, **972**, 81–93.

98 N. Kanlayakan, K. Kerdpol, C. Prommin, R. Salaeh, W. Chansen, C. Sattayanon and N. Kungwan, *New J. Chem.*, 2017, **41**, 8761–8771.

99 P. Selvaganapathi, S. Thirumaran and S. Ciattini, *J. Mol. Struct.*, 2017, **1148**, 547–556.

100 J. Hao and Y. Yang, *Org. Chem. Front.*, 2018, **5**, 1330–1341.

101 X. Li, D. Shan, C. Kim and Y.-A. Son, *Mol. Cryst. Liq. Cryst.*, 2016, **635**, 158–166.

102 W. Chansen, R. Salaeh, C. Prommin, K. Kerdpol, R. Daengngern and N. Kungwan, *Comput. Theor. Chem.*, 2017, **1113**, 42–51.

103 P. O. Hubin, A. D. Laurent, D. P. Vercauteren and D. Jacquemin, *Phys. Chem. Chem. Phys.*, 2014, **16**, 25288–25295.

104 S.-C. Lan and Y.-H. Liu, *Spectrochim. Acta, Part A*, 2015, **139**, 49–53.

105 G.-J. Zhao and K.-L. Han, *J. Phys. Chem. A*, 2007, **111**, 2469–2474.

106 Y. Yang, J. Zhao and Y. Li, *Sci. Rep.*, 2016, **6**, 32152.

107 Y. Houari, A. Charaf-Eddin, A. D. Laurent, J. Massue, R. Ziessel, G. Ulrich and D. Jacquemin, *Phys. Chem. Chem. Phys.*, 2013, **16**, 1319–1321.

108 L. Serrano-Andrés and M. Merchán, *J. Photochem. Photobiol., C*, 2009, **10**, 21–32.

109 Y. Saga, Y. Shibata and H. Tamiaki, *J. Photochem. Photobiol., C*, 2010, **11**, 15–24.

110 A. L. Sobolewski and W. Domcke, *Phys. Chem. Chem. Phys.*, 1999, **1**, 3065–3072.

111 P. Zhou, M. R. Hoffmann, K. Han and G. He, *J. Phys. Chem. B*, 2015, **119**, 2125–2131.

112 Y. Wang, Y. Shi, L. Cong and H. Li, *Spectrochim. Acta, Part A*, 2015, **137**, 913–918.

113 J. Zhao and Y. Zheng, *Sci. Rep.*, 2017, **7**, 44897.

114 G. Zucchi, T. Jeon, D. Tondelier, D. Aldakov, P. Thuéry, M. Ephritikhine and B. Geffroy, *J. Mater. Chem.*, 2010, **20**, 2114–2120.